Nanoscale Advances

ROYAL SOCIETY OF CHEMISTRY

PAPER

View Article Online
View Journal | View Issue

Check for updates

Cite this: *Nanoscale Adv.*, 2023, **5**, 1956

A humidity-resistant and room temperature carbon soot@ZIF-67 composite sensor for acetone vapour detection†

Lesego Malepe,[a] Tantoh Derek Ndinteh,[a] Patrick Ndungu[b] and Messai Adenew Mamo *[a]

Received 20th January 2023
Accepted 16th February 2023

DOI: 10.1039/d3na00050h

rsc.li/nanoscale-advances

Zeolitic imidazolate framework-67 (ZIF-67), carbon nanoparticles (CNPs), and the CNPs@ZIF-67 composite were prepared and used to fabricate sensors for the detection of acetone vapour. The prepared materials were characterized using transmission electron microscopy, powder X-ray diffraction, X-ray photoelectron spectroscopy, Raman spectroscopy and Fourier-transform infrared spectroscopy. The sensors were tested using an LCR meter under the resistance parameter. It was found that the ZIF-67 sensor did not respond at room temperature, the CNP sensor had a non-linear response to all analytes, and the CNPs/ZIF-67 sensor had an excellent linear response to acetone vapour and was less sensitive to 3-pentanone, 4-methyl-1-hexene, toluene and cyclohexane vapours. However, it was found that ZIF-67 improves carbon soot sensor sensitivity by 155 times, wherein the sensitivity of the carbon soot sensor and carbon soot@ZIF-67 sensor on acetone vapour was found to be 0.0004 and 0.062 respectively. In addition, the sensor was found to be insensitive to humidity and the limit of detection was 484 ppb at room temperature.

Open Access Article. Published on 16 Februari 2023. Downloaded on 16/10/2025 6:51:59 PTG.
This article is licensed under a Creative Commons Attribution-NonCommercial 3.0 Unported Licence.

1. Introduction

Acetone (CH_3COCH_3) is an organic compound that can easily evaporate at lower temperatures due to its high vapour pressure and low boiling point, 56 °C. It is widely utilised in paints, plastics, cosmetics, and detergents.[1] Severe inhalation of acetone vapour can cause bronchitis, eye inflammation and dizziness.[2] In certain environments, the detection of acetone vapour is very important for human health and safety, because high concentrations of acetone can affect organs such as the kidneys and liver.[3] Recently, the development of acetone gas sensors has received great interest in healthcare research, as it has become a new non-invasive method for the diagnosis of diabetes.[2] Clinical data have shown that the acetone concentration in exhaled breath of healthy individuals is approximately 0.3–0.9 ppm, while a concentration above 1.78 ppm may indicate a diabetic condition.[2,4,5] Hence, there is a need to design inexpensive, reproducible, fast-response, low-temperature working, highly selective and sensitive acetone gas sensors for biomedical applications,[6] or in various sectors such as the food industry, chemical processing, cosmetics, and human health safety within allied industries.

Over the years, semiconductor metal oxide (SMO) solid-state gas sensors have been widely investigated for the detection of volatile organic compounds (VOCs) and flammable toxic gases. The SMOs that have been widely applied as solid-state gas sensors include titanium dioxide, zinc oxide, tin dioxide, and tungsten trioxide.[7] These have been mainly used due to their good thermal stability, fast gas response–recovery times, low cost, and high sensitivity towards the gas of interest. Unfortunately, such sensors suffer from low selectivity toward the gas of interest when used with gas mixtures and typically have low sensitivity, especially at ppm to ppb concentration levels. In addition, their high operating temperature (about 240 to 400 °C) decreases the durability of the sensor and increases energy consumption.[7] Improving gas sensing characteristics of SMOs was carried out by introducing precious metals such as Pd, Pt, Ag, and Au.[8,9] However, the high working temperature remains a challenge. But the use of carbon nanomaterials such as graphene oxide,[10] carbon soot[11] or carbon nanotubes[12] can reduce the working temperatures of SMO-based gas sensors; however, they still suffer from poor gas selectivity and sensitivity.

Besides research on precious metals and carbon materials, other interesting research studies have focused on the use of zeolitic imidazolate frameworks (ZIFs), which have been used in gas sensing to improve selectivity due to porosity tunability, and their hydrophobic nature allows them to work at high humidity levels.[13] ZIF structures are made up of a central metal ion and imidazolate linkers arranged in a tetrahedral geometry similar to that found in zeolites.[14] ZIFs possess tremendous surface area and crystallinity and ZIF sensors are reported to have good

[a]Department of Chemical Science, University of Johannesburg, PO Box 17011, Doornfontein, 2028, Johannesburg, South Africa. E-mail: messaim@uj.ac.za
[b]Department of Chemistry, University of Pretoria, Private Bag X20, Hatfield, 0028, Pretoria, South Africa

† Electronic supplementary information (ESI) available. See DOI: https://doi.org/10.1039/d3na00050h

 © 2023 The Author(s). Published by the Royal Society of Chemistry

Open Access Article. Published on 16 Februari 2023. Downloaded on 16/10/2025 6:51:59 PTG.
This article is licensed under a Creative Commons Attribution-NonCommercial 3.0 Unported Licence.

selectivity, sensitivity and fast response recovery time; however, they operate at temperatures from 140 to 350 °C.[15] ZIF-67 is made up of cobalt (Co^{2+}) ions and 2-methylimidazolate, possessing cubic crystal symmetry.[16] ZIF-67 based sensor shows unresponsive behaviour towards VOCs at room temperature due to its high energy band gap and has been integrated with conducting materials to reduce the high working temperature.[17] In this study, ZIF-67 and carbon soot are used as a composite to detect acetone vapour at room temperature. Carbon soot is commonly known as carbon nanoparticles (CNPs) and possesses good conductivity, a high surface-to-volume ratio, and surface oxygen species that enhance gas sensing properties.[12] The CNPs/ZIF-67 composite solid-state gas sensor works at room temperature and relatively high humidity, has a low limit of detection and is highly sensitive toward acetone.

2. Experimental

2.1. Chemicals and reagents

Cobalt nitrate hexahydrate [$Co(NO_3)_2 \cdot 6H_2O$], 2-methylimidazole (99%), *N*, *N*-dimethylformamide (DMF, 99.5%), ethanol (EtOH, 98%), acetone (CH_3COCH_3, 99.5%), cyclohexane (C_6H_{15}, 99%), 4-methyl-1-hexene (C_7H_{14}, 99.5%), 3-pentanone ($C_5H_{10}O$, 99%), and toluene (C_7H_8, 99.8%), were purchased from Merck (South Africa). Lighthouse candles were purchased at a local supermarket in Johannesburg, South Africa.

2.2. Synthetic methods

2.2.1 Preparation of carbon soot. Carbon soot was prepared using a pyrolysis method that was previously reported by Olifant *et. al*.[11] The carbon nanoparticles were collected using a ceramic cup placed above a burning candle. The distance between the candle flame and the ceramic cup was approximately 1 cm. The collected black carbon soot was left to cool at room temperature for 30 minutes and scrapped off the ceramic cup using a spatula and then kept in a glass vial until ready for further use. The carbon nanoparticles were used without purification.

2.2.2 Synthesis of ZIF-67. ZIF-67 was synthesised using a method reported by Garg *et. al*.[17] First, 0.45 g cobalt nitrate hexahydrate [$Co(NO_3)_2 \cdot 6H_2O$] and 5.5 g 2-methylimidazole [$C_4H_6N_2$] were added into 3 and 20 mL deionised water respectively. The two solutions were then mixed together and stirred for two hours at room temperature to allow the formation of purple-coloured precipitates. The precipitates were then collected and washed several times through centrifugation with water and ethanol interchangeably to remove the presence of impurities. ZIF-67 precipitates were dried at 80 °C for 24 h in a vacuum oven.

2.2.3 Sensor fabrication. Three sensors were prepared for the detection of selected VOCs (acetone, 3-pentanone, cyclohexane, 4-methyl-1-hexene, and toluene). In separate vessels, 15 mg of ZIF-7 and 15 mg of CNPs were dispersed in 6 mL of DMF and stirred for 24 h to prepare sensor 1 and sensor 2 respectively. Sensor 3 was prepared by mixing 15 mg of CNPs and 15 mg of ZIF-67 and dispersing in 6 mL DMF (1 : 1 mass ratio of CNPs@ZIF-67). Our sensors are fabricated using gold-plated-interdigitated electrodes designed to have 18 paired lines of 7.9 mm long made up of gold, and the lines have a spacing of 0.1 mm. An aliquot of 7 μL was used from each prepared solution and drop coated on its respective interdigitated gold electrode and allowed to dry at room temperature. The dried film on the electrode was kept in a vacuum desiccator for over 72 hours to remove any remaining solvent.

2.2.4 Gas sensing setup. All the prepared solid-state gas sensors were investigated in the same setup (see Fig. 1). The prepared gas sensor was placed inside a 20 L round bottom flask and connected to an E4980A Keysight LCR meter. The round bottom flask had a pipe connected to a vacuum pump and another pipe introducing atmospheric air during the removal of any gas. An LCR meter was connected to a display monitor. In five trials, 1, 2, 3, 4, and 5 μL of VOCs were injected into the round bottom flask with a contact time of 10 min for each injection. Between each trial, the exposed vapour was flushed out using a vacuum pump (2 minutes of pump time) and then a rest period of 3 minutes was allowed before the next trial. During the injection of the liquid analyte, the VOCs quickly evaporate due to the high vapour pressure of the analyte liquid. The following formula (eqn (1)) was used to calculate the vapour concentration of the VOCs:

$$C = \frac{22.4pTV_s}{273M_rV} \times 1000, \quad (1)$$

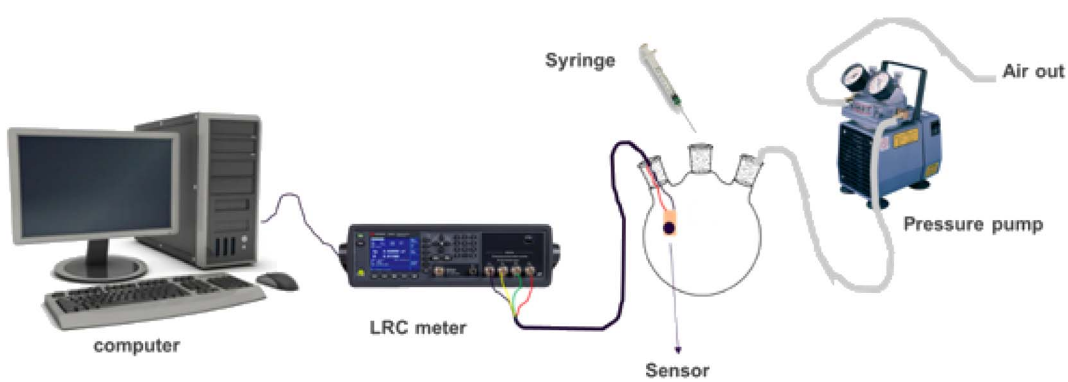

Fig. 1 Gas sensing setup.

Open Access Article. Published on 16 Februari 2023. Downloaded on 16/10/2025 6:51:59 PTG.
This article is licensed under a Creative Commons Attribution-NonCommercial 3.0 Unported Licence.

where C is the vapour concentration (ppm), p is the density of the liquid analyte (g cm^{-1}), T is the temperature (K), V_s is the volume injected into the 20 L volumetric flask (μL), M_r is the molar mass of the liquid analyte and V is the volume of the volumetric flask (L).[18]

2.2.5 Sensor's response and recovery tests. The gas sensor's response time was defined as the time needed for the sensor to reach a 90% maximum response before it reaches the saturated (plateau) state, while recovery time was defined as the 90% time needed for the sensor to reach its baseline during the removal of the gas exposed from its plateau.

2.2.6 *In situ* FTIR-online LCR meter measurement. The *in situ* FTIR-LCR meter set-up was followed as reported.[11] IR spectra were recorded using an FTIR instrument (PerkinElmer Spectrum 100) with a resolution of 4 cm^{-1} and 16 scans. A gas cell is a cylindrical cell (approx. 110 mL volume) fitted with two KBr windows at both ends. The vessel with two inlets for the sample injection and sensor electrical connection was placed at the centre with a sensor positioned on the upper wall of the cell in such a way that the IR beam passes through the windows without being blocked. The sensor was connected to the LCR meter through two electrically insulated wires. During the measurement, the sensor was exposed to about 375 ppm of the analyte vapour and the vessel was kept closed throughout the experiment. FTIR spectra were recorded every 1 min, while the resistance measurements were taken continuously for each sensor for a total maximum time of 22 min.

2.2.7 Humidity tests. Humidity tests were performed using a modified setup of Fig. 1 at room temperature, wherein a humidity sensor and the gas sensor were both placed inside the sensing chamber. The humidity of the chamber was varied by carefully controlling the volume of water vapour from boiling water into the chamber. Thus, the sensor detected acetone vapour under various relative humidity conditions.

2.2.8 Selectivity test. A mixture of analytes was prepared by adding 1 millilitre of acetone, toluene, cyclohexane, 4-methylhexene and 3-pentanone to make 5 mL and mixing well using a shaker. 5 μL was taken from the mixture and injected into a 3-necked round bottom flask in the presence of the CNPs/ZIF-67 sensor to study the selectivity of acetone vapour.

2.2.9 Characterization techniques. The morphology of ZIF-67, CNPs and CNPs/ZIF-67 were investigated using high-resolution transmission electron microscopy (HRTEM) at an acceleration voltage of 200 kV, on a JEOL-TEM 2010 (Japan) using Gatan software wherein samples were loaded onto copper grids. Powder X-ray diffraction (PXRD) was performed using a Bruker D2 Phaser using a LynxEye detector with CuKα radiation at a wavelength of 0.154 nm. A Bruker Senterra laser Raman spectrometer fitted with a frequency-doubled Nd-YAG laser with a wavelength of 532 nm was used for Raman analysis. Fourier transform infrared spectroscopy (FTIR, Bruker-Alpha, Germany) was used to identify chemical functionalities on the materials.

3. Results and discussion

3.1. Materials characterization

Structural analysis of CNPs and CNPs/ZIF-67 was performed using PXRD (see Fig. 2). In the case of CNPs, two broad bands were observed at $2\theta = 25$ and 44° which are indexed to (002) and (101) crystal faces for graphitic carbon (ICDD: 04-018-7559) and characteristic of CNPs. Fig. 2b presents the PXRD pattern of CNPs/ZIF-67 showing diffraction peaks at $2\theta = 7°$, 10°, 13°, 15°, 17°, 18°, 22°, 25°, 27°, 30°, 31 and 32°, which were indexed to the crystal planes (011), (002), (012), (022), (013), (222), (014), (233), (134), (044), (244) and (235) respectively, the reflections of rhombic dodecahedron phase of ZIF-67.[19] Unfortunately, the two broad peaks from CNPs are not observed on the CNPs/ZIF-67PXRD diffraction pattern because the high-intensity peaks from crystalline ZIF-67 suppress the amorphous CNP peaks. The HRTEM and TEM-EDS results for CNPs, ZIF-67 and the CNPs/ZIF-67 composite are presented in Fig. 3. CNPs appear to be spherical with an average diameter between 20 and 30 nm and are highly agglomerated (see Fig. 3a). TEM-EDS shows that the CNPs are composed of carbon and oxygen only (see Fig. 3b). Fig. 3c shows that ZIF-67 possesses a hexagonal shape, the average crystal size is 100–160 nm, and the corresponding EDS spectrum has carbon and nitrogen peaks from 2-methylimidazole, cobalt peaks from the metal precursor, and oxygen likely from oxides on the material surface which agrees with the FTIR results. The EDS spectrum of the CNPs/ZIF-67 samples

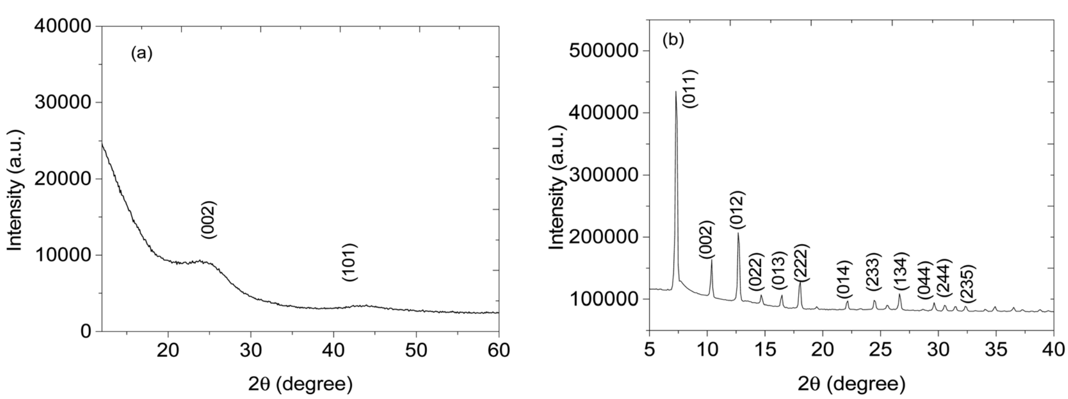

Fig. 2 XRD pattern of (a) carbon soot and (b) CNPs@ZIF-67.

 © 2023 The Author(s). Published by the Royal Society of Chemistry

Open Access Article. Published on 16 Februari 2023. Downloaded on 16/10/2025 6:51:59 PTG.
This article is licensed under a Creative Commons Attribution-NonCommercial 3.0 Unported Licence.

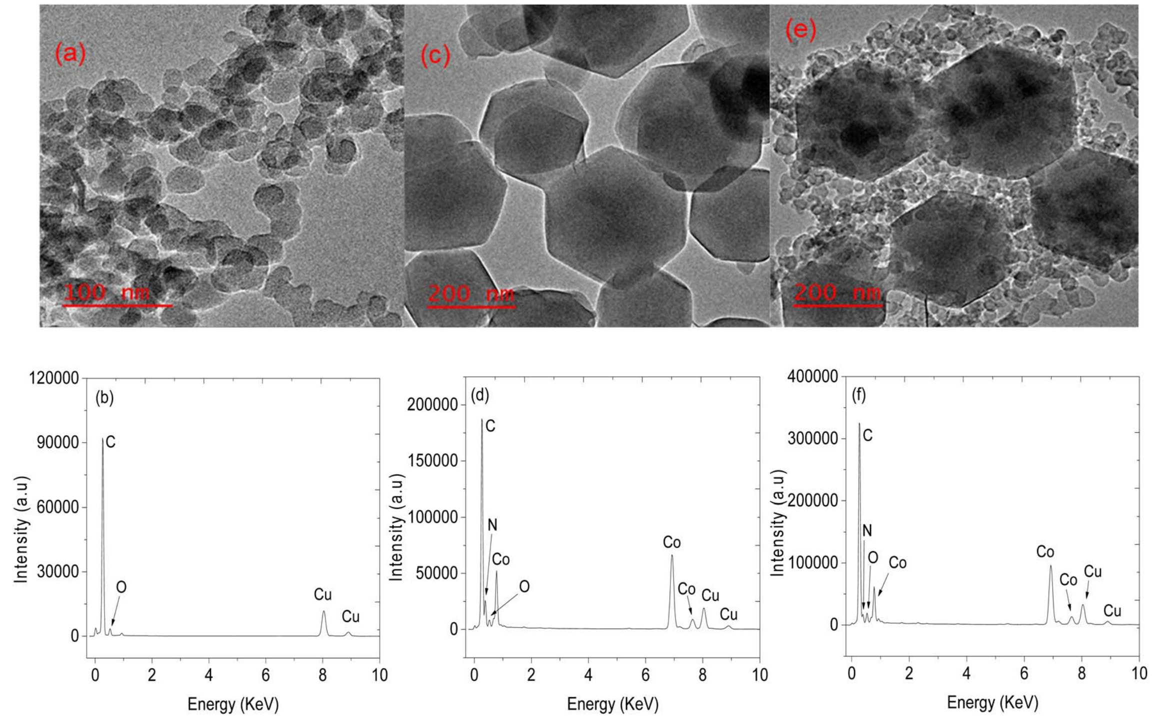

Fig. 3 TEM images of (a) CNPs, (c) ZIF-67 (e) CNPs/ZIF-67 and their respective EDS spectra, (b), (d) and (f).

possesses similar peaks to those found in the spectra of ZIF-67 and the CNPs as expected (Fig. 3f). The TEM image of the CNPs/ZIF-67 composite revealed that the CNP soot covers the surface of ZIF-67 (Fig. 3e), which likely plays a crucial role in improving the electrical conductivity of the nanocomposite and facilitated the gas sensing process.

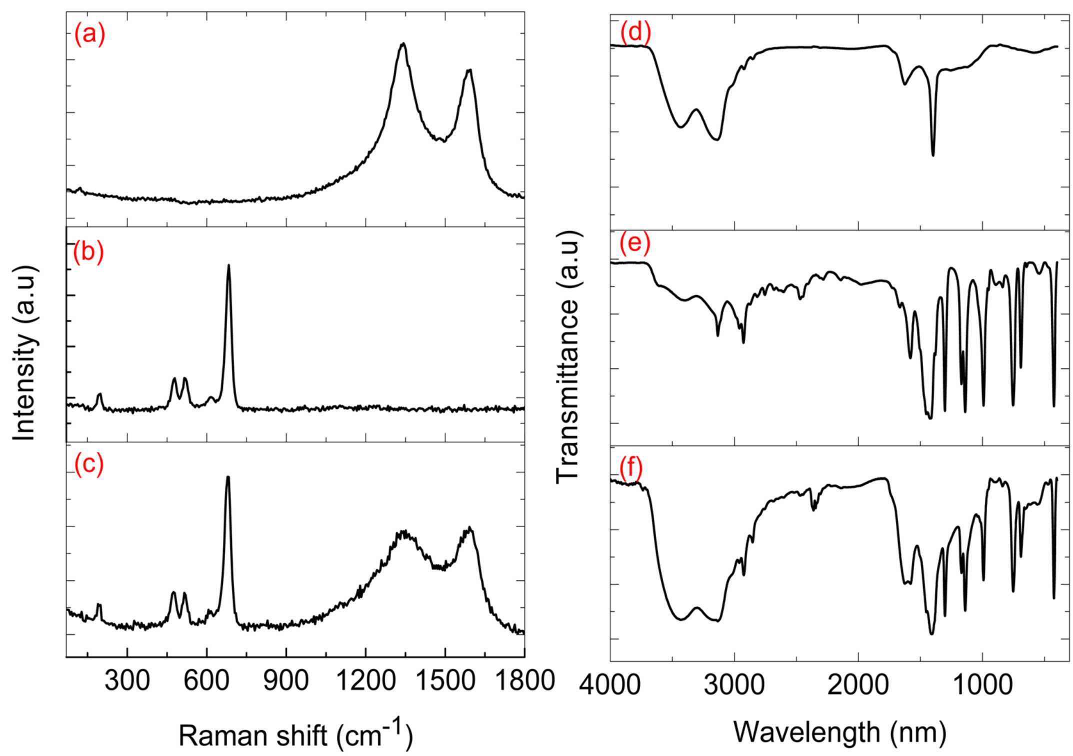

Fig. 4 The Raman patterns of (a) CNPs, (b) ZIF-67 and (c) CNPs@ZIF-67. The FTIR spectra of (d) CNPs, (e) ZIF-67 and (f) CNPs@ZIF-67.

© 2023 The Author(s). Published by the Royal Society of Chemistry

Open Access Article. Published on 16 Februari 2023. Downloaded on 16/10/2025 6:51:59 PTG.
This article is licensed under a Creative Commons Attribution-NonCommercial 3.0 Unported Licence.

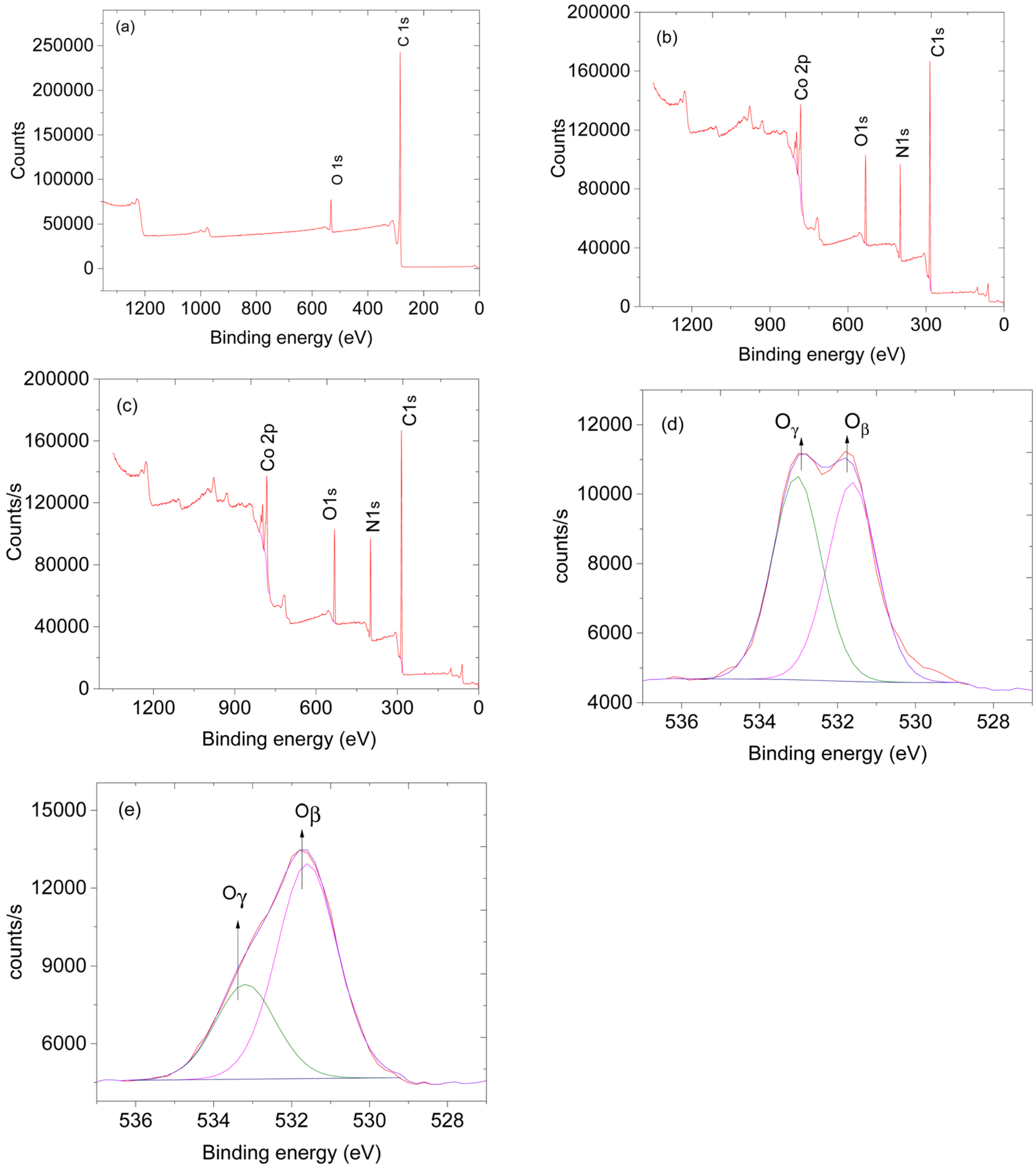

Fig. 5 XPS spectra and XPs survey of (a) CNTs, (b) ZIF-67 and (c) ZIF-67/CNPs and (d) O 1s of CNPs and (e) O 1s of ZIF-67.

Table 1 XPS O 1s oxygen species percentages

Materials	O_β	O_γ
CNPs	48.7%	51.7%
ZIF-67	58.8%	41.2%
CNPs@ZIF-67	74.4%	25.6%

Fig. 4a presents the CNP Raman spectra, which exhibited two broad peaks positioned at 1350 and 1555 cm^{-1} and are assigned to the characteristic D and G bands, for carbon nanomaterials. The D band represents defects within the graphene sheets that make up the CNPs, and the G band is due to the graphitic nature of the carbon nanoparticles.[18] Raman spectroscopy is often deployed to study carbon nanomaterials, typically by calculating the integrated intensity ratio between the D and G bands (I_D/I_G). Perumbilavil *et al.* showed that the I_D/I_G ratio increases from graphite (0.70) to graphene oxide (1.03), due to the oxygen species present in the graphene oxide, and reduced graphene oxide had an I_D/I_G ratio of 0.93 indicating that there was a removal of oxygen species from graphene oxide.[20] The I_D/I_G of our CNPs was 1.08 and that of the I_D/I_G ZIFs-67/CNPs was 1.00, indicative of the disordered nature of the CNPs and the probable presence of oxygen species on the CNPs. As shown in Fig. 4b, the ZIF-67 spectra exhibited five Raman peaks, 198, 477, 524, 616 and 684 cm^{-1} which are characteristic of cobalt-ZIF. The Raman peaks at 477 and 684 cm^{-1} are typically observed with ZIF-67, whereby 477 cm^{-1} is attributed to the Co–N bond and the vibration mode at 684 cm^{-1} is assigned to the 2-methylimidazolate ligand.[21] The Raman signals positioned at

 © 2023 The Author(s). Published by the Royal Society of Chemistry

Open Access Article. Published on 16 February 2023. Downloaded on 16/10/2025 6:51:59 PTG.
This article is licensed under a Creative Commons Attribution-NonCommercial 3.0 Unported Licence.

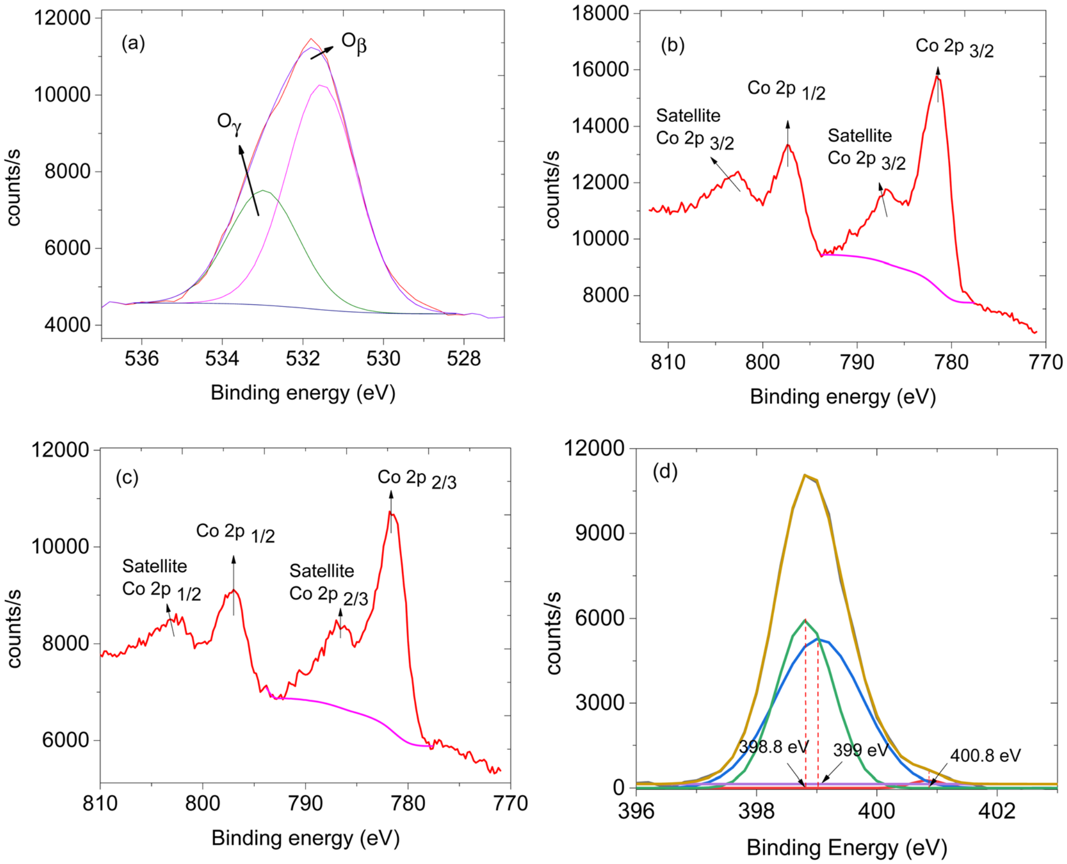

Fig. 6 XPS spectra, (a) O 1s of ZIF-67/CNPs, (b) Co 2p of ZIF-67, (c) Co 2p of ZIF-67/CNPs and (d) N 1s of ZIF-67.

198, 524 and 616 cm^{-1} are all assigned to F_{2g} and the signal at 477 cm^{-1} and the strongest signal at 684 cm^{-1} are assigned to A_1 and E_g mode respectively.[22,23] FTIR spectra presented in Fig. 4d–f show that the CNPs (Fig. 4d) had a broad peak at 3555 cm^{-1} representing O–H stretching, 3233 cm^{-1} and 3129 cm^{-1} for the C–H and the peak occurring at 1374 cm^{-1} is for C–O–C bonding character. The ZIF-67 FTIR spectrum (Fig. 4e) showed N–H stretching peaks at 3404 cm^{-1}, peaks at 3128 cm^{-1} and 2907 cm^{-1} for C–H stretching from the methyl group on the imidazole ring, a C=N peak at 1572 cm^{-1}, peaks from 1428–667 cm^{-1} due to the stretching of the imidazole ring, and a peak at 414 cm^{-1} due to Co–N stretching, confirming the bond between cobalt and the linker. The presence of two broad peaks positioned at 3233 cm^{-1} and 3129 cm^{-1} confirms the presence of CNPs within the CNPs/ZIF-67 composite (Fig. 4f), and complements the Raman spectra results.

The availability of oxygen species on the surface of the sensing material plays a crucial role in facilitating the effectiveness of the sensor.[24] Thus, XPS analysis was performed to study the oxygen species on the materials. XPS survey spectra of CNTs, ZIF-67 and CNPs:ZIF-67 revealed the presence of carbon (C), nitrogen (N), oxygen (O) and cobalt (Co) (see Fig. 5a–c). The deconvoluted spectra as aligned for the O 1s XPS spectra of CNPs, ZIF-67 and the CNPs:ZIF-67 composite exhibit oxygen species O_β and O_γ occurring at approximately 531.9 and 533.2 eV respectively (see Fig. 5d and e). The O_β shows the presence of adsorbed oxygen species and O_γ represents the adsorbed species on the sample.[25] Interestingly, the percentage of O_β species of the composite has increased from about 59% to 74% and that of the O_γ decreased from 41% to about 26% (See Table 1). The changes in the concentration of reactive oxygen species particularly, the O_β, are the ones involved in the sensing mechanism during the total decomposition of organic compounds. After deconvoluting the Co 2p peaks, four characteristic peaks were observed; peaks at 781.2 and 786.2 eV are attributed to Co $2p_{3/2}$ while, 7997.1 and 802.1 eV are assigned to Co $2p_{1/2}$ spin-orbital splittings (see Fig. 6b and c).[26,27] Thus the existence of the main and the satellite peaks Co $2p_{2/3}$ and Co $2p_{1/2}$ indicates the existence of Co^{3+} and Co^{2+} within ZIF-67 and CNPs:ZIF-67 (see Fig. 6b).[28,29] The peak at 398.8 eV was assigned to the pyridinic N while 399.0 eV was the pyrrolic N and 400.8 eV was the quaternary N (see Fig. 6d).[28,29]

3.2. Sensing studies

3.2.1 Gas response and sensitivity. The change in the electrical response was investigated during the interaction between all prepared solid-state gas sensors and the gaseous analytes (see Fig. S1† for the set-up) by injecting the analyte liquid in a glass chamber. All the tests were performed at room temperature and the change in the electrical response was recorded in terms of relative resistance Δ*R*. The sensitivity of the

Open Access Article. Published on 16 February 2023. Downloaded on 16/10/2025 6:51:59 PTG.
This article is licensed under a Creative Commons Attribution-NonCommercial 3.0 Unported Licence.

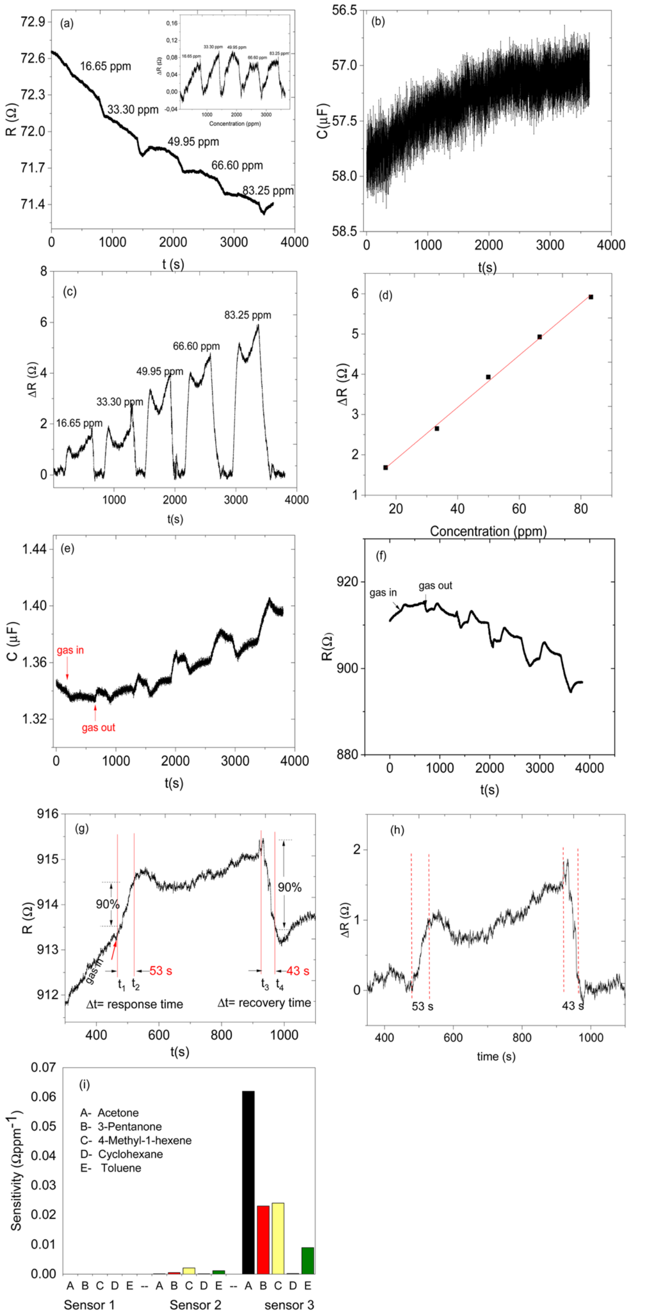

Fig. 7 (a) Transient response of sensor 2 towards acetone vapour (inset: relative response of sensor 2 towards acetone vapour) and (b) a capacitance transient response of sensor 2 towards acetone vapour, (c) relative resistance response curve of sensor 3 towards acetone vapour, (d) a calibration curve of sensor 3 towards acetone vapour, (e) a capacitance transient response of sensor 3 towards acetone vapour, (f) a resistance transient response of sensor 3 towards acetone vapour, (g) transient response–recovery graph and (h) relative response–recovery graph and (i) sensitivity in the bar graph.

sensors is calculated using the equation, $S = \frac{\Delta R}{\Delta C}$, where S is the sensitivity in Ω ppm^{-1}, ΔR is the change in electrical resistance in Ω and ΔC is the change in concentration of the analytes in ppm.

Sensor 1 made up of only ZIF-67 showed no meaningful response towards all the analyte vapours, only a high noise-to-signal ratio; this might be because ZIF-based sensors respond only at higher temperatures.[13,15] Sensor 2 (based on only the CNPs) showed a response to all exposed analytes (acetone, 3-pentanone, 4-methyl-1-hexene, toluene and cyclohexane) and after exposure, the sensor returned to its baseline after the removal of an exposed analyte. Unfortunately, there is no linear relationship between the increases in the concentration of the analyte vapour and relative resistance response and a capacitance transient response (Fig. 7a and b) and the sensor displayed low sensitivity towards all the analyte vapours. Sensor 3 (CNPs/ZIF-67), however, performed well with a linear increase in the relative response as the concentrations increased (Fig. 7c and d). The sensor showed an increase in relative resistance responses during its contact with analyte vapour and recovers back to its baseline when the analyte vapour is removed. On the other hand, the capacitance and the resistance transient response of sensor 3, as shown in Fig. 7e and f, towards acetone vapour showed signal drift due to the chemical and physical environment around the sensors.[30,31] Although sensor signal drift quite commonly occurs in gas sensors it can be compensated by using mathematical models.[32] The introduction of CNPs into ZIF-67 (sensor 3) improved the sensitivity of the sensor (>155×) when compared to sensor 2. Sensor 3 responds strongly toward acetone and responded poorly toward other analytes (3-pentanone, 4-methyl-1-hexene, toluene and cyclohexane).

The comparative sensitivity of all analytes was studied (Fig. 7i). Sensor 3 showed high sensitivity towards acetone vapour at 0.062 Ω ppm^{-1}, followed by 4-methyl-1-hexene at 0.024 Ω ppm^{-1}, 3-pentanone at 0.023 Ω ppm^{-1}, toluene 0.009 Ω ppm^{-1} and no response value with cyclohexane vapour. Sensor 3 showed 2.7 times more sensitivity for acetone vapour when compared to 4-methyl-1-hexane vapour (Fig. 7i). In terms of response and recovery time, sensor 3 responded to the acetone vapour in 53 seconds and recovered back to its baseline in 43 seconds (Fig. 7g). The response time of the fabricated sensor is longer than the recovery time. This mainly depends on two factors, the diffusion process and reaction limited process on the surface of the electrodes. In most cases, the diffusion process of the analyte gases is much slower compared to the reaction kinetics; therefore the time required for the sensing process depends only on gas diffusion through the sensing layer.[33–36] On the other hand, the total number of the analyte molecules immobilized at the active sites is directly proportional to the concentration of the analyte molecules in the chamber, which depends only on the time required for the analyte molecules to diffuse through and the effective diffusion constant of the analyte molecules. In the case of diffusion, which is instantaneous compared to adsorption kinetics, the concentration of the analyte molecules at any point becomes independent of time and the response at a particular time depends only on the number of adsorbed molecules on the active sites, which is again directly proportional to the analyte molecule concentration. Therefore, the reason why our sensor was relatively slow to respond is due to that the analyte

© 2023 The Author(s). Published by the Royal Society of Chemistry

Open Access Article. Published on 16 February 2023. Downloaded on 16/10/2025 6:51:59 PTG.
This article is licensed under a Creative Commons Attribution-NonCommercial 3.0 Unported Licence.

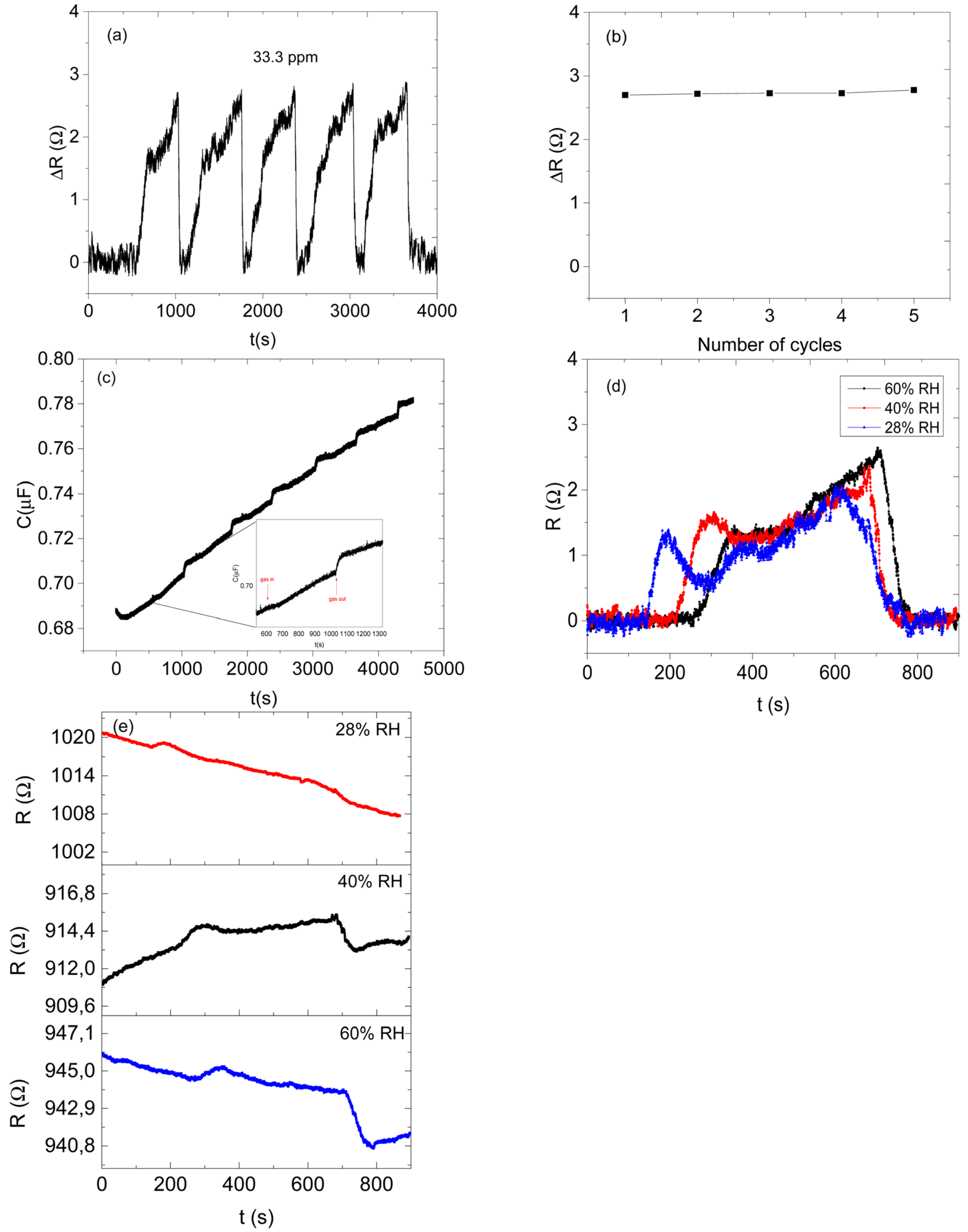

Fig. 8 (a) Repeatability of the CNPs/ZIF-67 sensor on acetone vapour, (b) its maximum amplitude of the response peaks and (c) a capacitance transient response repeatability test of the sensors, (d) acetone vapour relative response at different relative humidities and (e) transient acetone vapour response at different relative humidities.

molecules are slower to diffuse through the sensing material. The reason why the recovery time is faster than the response time is that the concentration of the analyte was dropped to a lower level due to the air being flashed through the chamber.

3.2.2 Sensor reproducibility and its humidity test. The stability (reproducibility) of sensor 3 (CNPs/ZIF-67) was studied for the detection of acetone vapour (Fig. 8a and b). The sensor showed almost the same responses for 5 cycles at 33.3 ppm, which proves good stability and repeatability. Furthermore, the sensor maintained its stability without losing its response–recovery ability and sensitivity (Fig. 8a). However, the capacitance transient response showed a signal drift as shown in Fig. 8c. This is due to, as explained earlier, the chemical and physical changes around the sensing materials. The inset of

Open Access Article. Published on 16 Februari 2023. Downloaded on 16/10/2025 6:51:59 PTG.
This article is licensed under a Creative Commons Attribution-NonCommercial 3.0 Unported Licence.

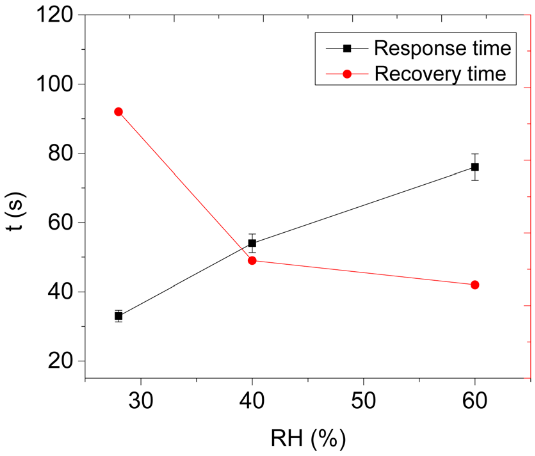

Fig. 9 The response and recovery times *versus* relative humidity.

Fig. 8c shows that the sensor responded apart from the response drifting away from the baseline.

It has been widely reported that changes in humidity can tremendously affect the performance of gas sensors.[37] Under higher humidity conditions, water molecules usually get trapped in sensing materials and this leads to the drifting of the response of the sensor. Trapped water molecules in the active sites of sensing materials delay any interactions between the gas analyte and sensing material, and thus the response of the targeted analyte might be insignificant.[38]

Therefore, the effect of humidity on the detection of acetone vapour using the CNPs/ZIF-67 sensor was investigated. The sensor was exposed to acetone vapour (at 16.65 ppm) in three trials at different relative humidities, 28%, 40%, and 60% (Fig. 8d). The maximum response of acetone vapour at these respective RH was 1.6, 1.5, and 1.3 Ω, respectively (Fig. 8d–e). According to the results, there is a slight change in the response of about 0.3 Ω as RH increased from 28% to 60%. Interestingly, the sensor maintained the shape of the response curve and response–recovery characteristics, and this demonstrates that the presence of water molecules had a small effect on the CNPs/ZIF-67 sensor (Fig. 8d). The presence of water vapour in the system affected the response and recovery times, with the response time being delayed over twice and the recovery time being less than halved as the humidity increased. The delay in response time at high humidity implies that the presence of water vapour in the system might create competition between the acetone and water molecules for the active sites of the sensor. The quicker recovery time may indicate that the interaction of the water vapour with the sensing materials is weak and not a strong or permanent bond (Fig. 9 and Table 3).

Table 3 Response and recovery times of sensor 3 at different humidities

Relative humidity (RH)	Response time (s)	Recovery time (s)
28%	33	98
40%	54	49
60%	76	42

The response–recovery time of the CNPs/ZIF-67 sensor at room temperature is fast when compared to those of previously reported work (Table 2), for example, the SnO_2-reduced graphene oxide and V_2O_5 nanoneedle-based sensors.

3.2.3 Acetone sensing mechanism. The CNPs/ZIF-67 composite sensor is controlled by surface interaction based on the change in resistance that is believed to be more similar to that in n-type semiconductor metal oxides.[11] Thus, CNPs/ZIF-67 uses adsorption–desorption sensing mechanism. First, the surface of the CNPs/ZIF-67 sensor chemisorbs the oxygen molecules when exposed to atmospheric conditions, capturing the electrons from the conduction band of ZIF-67 and ionising them into highly reactive oxygen species (O_2, O_2^{2-} and O^{2-}).[43] Consequently, the electron depletion layer formation causes the band to bend and results in the formation of a potential barrier and the sensing material turns out to have high resistance.[43] During the sensing process, acetone vapour interacts with the reactive oxygen species on the surface of CNPs/ZIF-67 and forms carbon dioxide and water vapour as by-products. Subsequently, the electrons are released back into the conduction band of the sensing material and the bent band returns to its original state.[43] The width of the electron depletion layer and the resistance of the material decrease; this behaviour is typical of p-type semiconductors. The CNP sensor responded to all analytes due to the presence of molecular oxygen species on CNPs formed during the synthesis of the carbon nanomaterial. These adsorbed molecular oxygens are highly reactive and similar findings were reported on carbon black at 300 K.[44] Raman analysis revealed that CNPs are highly disordered (see Fig. 4a) and have high charge activity transfer that promotes the chemisorption of the acetone vapour and increases the gas responses of the sensors.[45,46] The presence and characteristics of the oxygen

Table 2 Sensing materials and their sensing performances towards acetone vapour

Materials	Res/rec time	LOD	Working temp.	Response	Ref.
$ZnFe_2O_4$ microspheres	7.5/200 s	1 ppm	215	6.5 at 10 ppm	39
3.0 wt% Cu-doped α-Fe_2O_3 porous nanotubes	5 s/18 s	100 ppb	164	12 at 5 ppm	40
In_2O_3–CuO	13/20 s	50 ppm	370	5 at 0.5 ppm	41
V_2O_5 nanoneedles	73/88 s	1.7 ppm	Room temp	2.37 for 140 ppm	42
ZnO@ZIF-71(Co)	71/53 s	50 ppb	250	5.7 at 0.5 ppm	43
CNPs@ZIF-67	53 s/43 s	484 ppb	Room temp	2 at 16.7 ppm	This work

 © 2023 The Author(s). Published by the Royal Society of Chemistry

Open Access Article. Published on 16 Februari 2023. Downloaded on 16/10/2025 6:51:59 PTG.
This article is licensed under a Creative Commons Attribution-NonCommercial 3.0 Unported Licence.

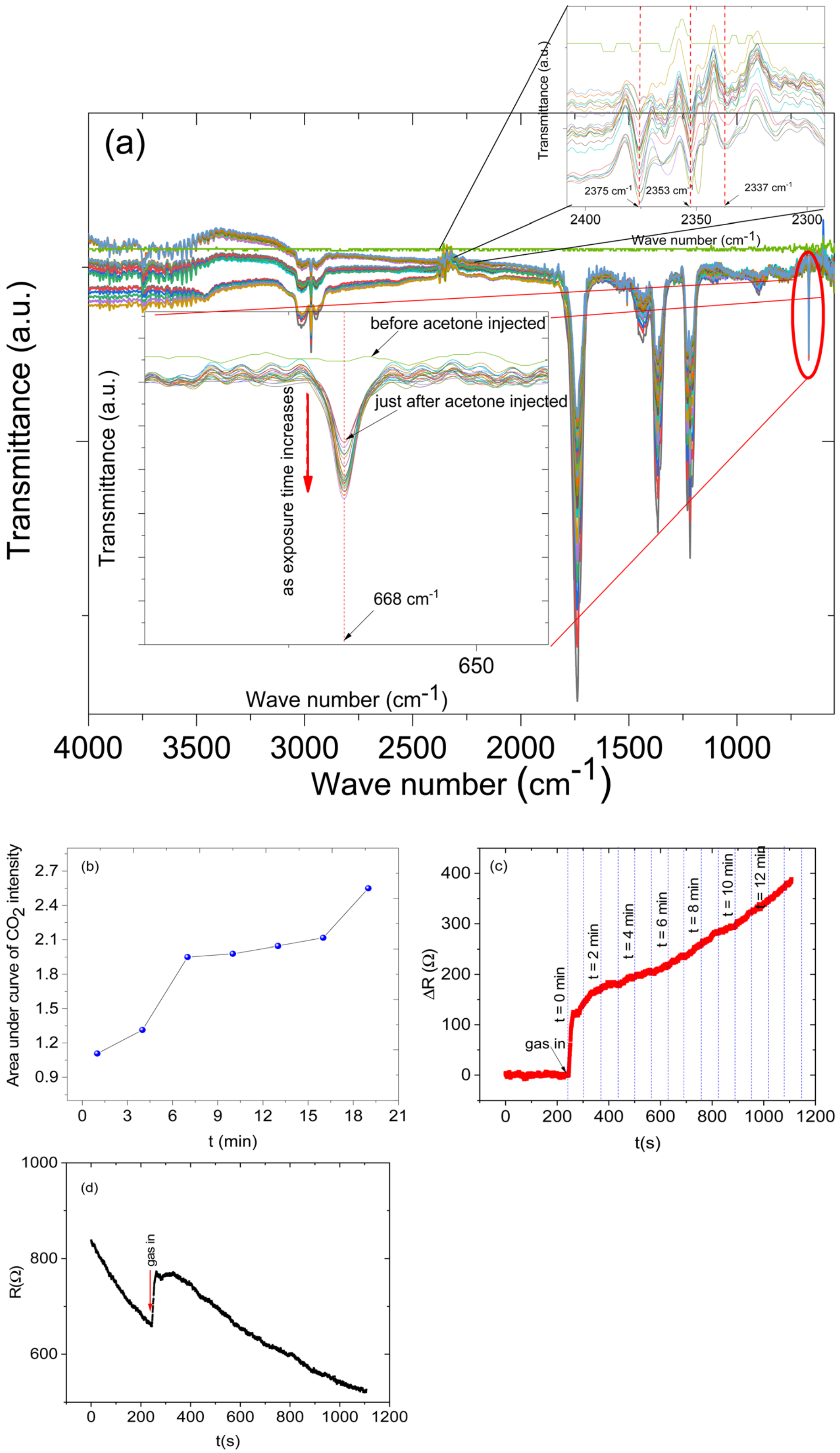

Fig. 10 (a) *In situ* FTIR: (b) areas under the curve of the CO_2 IR intensities against time (selected) (min), (c) the relative response of the sensor during the *in situ* FTIR coupled with LCR meter measurement and (d) transient response of the sensor during the *in situ* FTIR coupled with LCR meter measurement.

Open Access Article. Published on 16 Februari 2023. Downloaded on 16/10/2025 6:51:59 PTG.
This article is licensed under a Creative Commons Attribution-NonCommercial 3.0 Unported Licence.

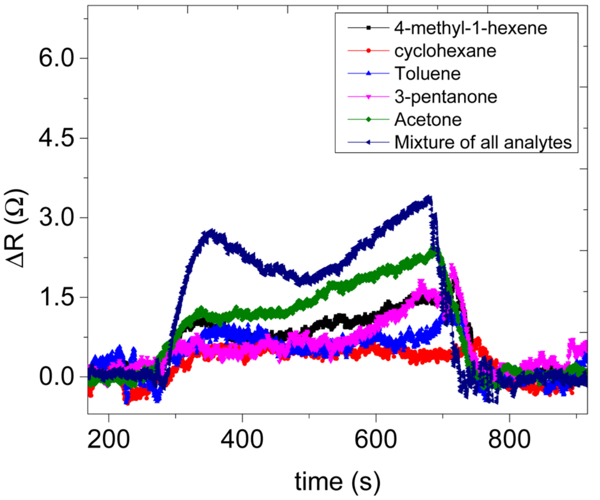

Fig. 11 Static response–recovery curve of sensor 3.

species on CNPs were confirmed using XPS characterisation (Fig. 5d and Table 1). These reactive oxygen species on the sensor catalyse the decomposition of acetone into carbon dioxide and water. The synergistic effect of the CNPs and ZIF-67 in the CNPs/ZIF-67 material results in room temperature operations of the sensor. This synergistic effect is first due to the increase of $O_β$ species of the composite which increased from about 59% to 74% (See Table 1). It is known that the type of oxygen adsorbed on the sensor determines whether the sensing mechanism will undergo total oxidation or oxidative dehydrogenation.[46,47]

Furthermore, to understand the sensing mechanism of the prepared sensor we set up an *in situ* FTIR-coupled with LCR meter online measurement (See Fig. 10). While the sensor was exposed to the analyte vapours both the response and the FTIR spectra were recorded. The FTIR spectra were recorded every 1 min for 22 min. In this measurement, we focused on specific CO_2 IR bands that can give us evidence of the sensing mechanism.

The *in situ* FTIR-LCR meter results indicate that new distinct IR bands have emerged during the exposure of the sensor to the analyte. The IR band in the region of 2377 to 2349 cm^{-1} is due to CO_2 asymmetric stretching (Fig. 10a inset) and a band at 668 cm^{-1} was assigned to the CO_2 bending mode.[48,49] This particular band doesn't overlap with other bands and is important since it can give us information about the reaction on the surface. It is possible to see the CO_2 bending mode (at 668 cm^{-1}) intensity increase as the analyte molecules' exposure time increases (see Fig. 10a inset). The intensity of the band at 668 cm^{-1} before the analyte molecule was injected was flat and as time passed the intensity increased. The increase in the intensity of the CO_2 IR band is the result of increasing the concentration of CO_2 in the gas cell and also this can be related to the deep oxidation of the acetone on the surface of the sensing materials and then the desorption of carbon dioxide gas molecules from the surface of the sensors. Similarly, the sensor response also increases as the exposure time increases (Fig. 10c).

Moreover, the CO_2 IR intensities were fitted with Gaussian curves and the areas under the curves were calculated and plotted against the exposure time (Fig. 10b). The result shows that indeed the concentration of CO_2 increases as the exposure increases.

Therefore based on the result from the coupled *in situ* FTIR-LCR meter, the following sensing mechanism between oxygen reactive species and acetone vapour was proposed (2)–(5):

$$O_2\ (\text{gas}) \rightarrow O_2\ (\text{ads}) \tag{2}$$

$$O_2\ (\text{gas}) + e^- \rightarrow O_2^-\ (\text{ads}) \tag{3}$$

$$O_2^-\ (\text{ads}) + e^- \rightarrow 2O^-\ (\text{ads}) \tag{4}$$

Acetone vapour

$$C_3H_6O\ (\text{gas}) + 9O^- \rightarrow 3CO_2 + 3H_2O + 9e^- \tag{5}$$

3.2.4 Limit of detection. The relationship between the electrical response and acetone vapour concentration from 16.65 to 83.25 ppm was approximately linear (Fig. 7d) and the correlation coefficient (R^2) and slope of the linear fit were 0.99 and 0.062 Ω ppm^{-1} respectively. The LOD was approximated to be 484 ppb and was calculated using the formula LOD = 3 × RMS/slope,[18,50] where RMS was the standard deviation and the RMS was found to be 0.001.

3.2.5 Selectivity studies. The selectivity of the CNPs/ZIF-67 sensor (sensor 3) in the detection of acetone vapour in the presence of 3-pentanone, 4-methyl-1-hexene, toluene and cyclohexene vapours was investigated (see Fig. 11). All five analytes (acetone, toluene, cyclohexane, 3-pentanone and 4-methyl-1-hexene) were mixed together and the analyte mixture was detected. The response of the analyte mixture vapour was compared to the response of the targeted acetone vapour. The maximum response of the acetone vapour is 2.41 Ω, while the maximum response of the analyte mixture is 3.29 Ω, and the other analytes with poor responses are cyclohexane (0.31 Ω), 4-methyl-1-hexene (1.42 Ω), 3-pentanone (1.50 Ω), and toluene (0.65 Ω). The volume of the tested mixture was 5 μL (see preparation methods), while the volume of the tested targeted acetone was 1 μL, and then the mixture response did not overshoot and the response is almost the same in magnitude as that of acetone vapour. The mixture's response is slightly higher due to the interferences possessed by the vapour interaction from the other vapours. The response time of acetone is 53 s. Meanwhile, the response time of the mixture is 63 s. The delay in response from the mixture could be due to that the untargeted analytes (toluene, cyclohexane, 4-methyl-hexene and 3-pentanone vapours) are blocking some active sites on the sensor which results in a delay in response from our targeted acetone vapour.

4. Conclusions

In summary, carbon soot (CNPs) was prepared from pyrolysis of household wax, ZIF-67 was prepared from the sol–gel method

© 2023 The Author(s). Published by the Royal Society of Chemistry

Open Access Article. Published on 16 Februari 2023. Downloaded on 16/10/2025 6:51:59 PTG.
This article is licensed under a Creative Commons Attribution-NonCommercial 3.0 Unported Licence.

and the CNPs/ZIF-67 composite was prepared from physical mixing. All the prepared materials were characterized using TEM, FTIR, XPS, Raman spectroscopy and XRD. All sensors were tested at room temperature. The CNPs/ZIF-67 sensor improved the sensitivity of the CNP sensor by 155 times during the detection of acetone vapour while the ZIF-67 sensor did not respond to any analyte. And the CNPs/ZIF-67 sensor was found to be highly sensitive to acetone vapour and less sensitive to cyclohexane, 3-pentanone, 4-methyl-1-hexene, and toluene vapours. In addition, the sensor was found to be humidity insensitive and had fast response–recovery times and the LOD was found to be 484 ppb on the detection of acetone vapour. Thus the CNPs/ZIF-67 sensor is a promising candidate for a fast, portable, non-invasive, and inexpensive diabetes diagnosis method and to maintain good health in high acetone vapour environments.

Author contributions

L. Malepe performed all the experiments and investigations and wrote the manuscript. M. A. Mamo conceived the idea and guided and reviewed the manuscript. P. Ndungu and D. T. Ndinteh are responsible for providing resources, editing, and reviewing the manuscript.

Conflicts of interest

There are no conflicts to declare. The manuscript was written through the contributions of all authors.

Acknowledgements

Lesego Malepe thanks the University of Johannesburg for financial assistance. All authors acknowledge the University of Johannesburg for financial assistance. The support of the Centre for Nanomaterials Science Research at the University of Johannesburg is also gratefully acknowledged.

Notes and references

1 Y. Obeidat, A. M. Rawashdeh, A. Hammoudeh, R. Ai-Assi, A. Dagamseh and Q. Qananwah, Acetone sensing in liquid and gas phases using cyclic voltammetry, *Sci. Rep.*, 2020, **12**, 11010.

2 J. Guo, D. Zhang, T. Li, J. Zhang and L. Yu, Green light-driven acetone gas sensor based on electrospinned CdS nanospheres/Co_3O_4 nanofibers hybrid for the detection of exhaled diabetes biomarker, *J. Colloid Interface Sci.*, 2021, **606**, 261–271.

3 F. Meng, J. Hu, C. Liu, Y. Tan and Y. Zhang, Highly sensitive and low detection limit of acetone gas sensor based on porous $YbFeO_3$ nanocrystallines, *Chem. Phys. Lett.*, 2021, **780**, 138925.

4 O. Alkedeh and R. Priefer, The ketogenic diet: Breath acetone sensing technology, *Biosensors*, 2021, **11**, 26.

5 O. B. Crofford, R. E. Mallard, R. E. Winton, N. L. Rogers, J. C. Jackson and U. Keller, Acetone in breath and blood, *Trans. Am. Clin. Climatol. Assoc.*, 1977, **88**, 128–139.

6 Y. T. Ma, S. Y. Ma, J. Tang, Z. G. Wu, J. Shi, Y. Zhao and S. T. Pei, One-pot hydrothermal method synthesised SnS/rGO nanocomposite under PVDF bonding for high-performance acetone gas sensor, *Mater. Sci. Eng. B*, 2020, **263**, 114861.

7 A. Mirzaei, S. S. Kim and H. W. Kim, Resistance-based H_2S gas sensors using metal oxide nanostructures: a review of recent advances, *J. Hazard. Mater.*, 2018, **357**, 314–331.

8 G. Tofighi, D. Degler, B. Junker, S. Müller, H. Lichtenberg, W. Wang, U. Weimar, N. Barsan and J. D. Grunwaldt, Microfluidically synthesized Au, Pd and AuPd nanoparticles supported on SnO_2 for gas sensing applications, *Sens. Actuators, B*, 2019, **292**, 48–56.

9 J. Liu, L. Zhang, J. Fan, B. Zhu and J. Yu, Triethylamine gas sensor based on Pt-functionalized hierarchical ZnO microspheres, *Sens. Actuators, B*, 2021, **331**, 129425.

10 H. F. Fei, G. Wu, W. Y. Cheng, W. J. Yan, H. J. Xu, D. Zhang, Y. F. Zhao, Y. H. Lv, Y. H. Chen, L. Zhang, C. O. Coileain, C. L. Heng, C. R. Chang and H. C. Wu, Enhanced NO_2 sensing at room temperature with graphene *via* monodisperse polystyrene bead decoration, *ACS Omega*, 2019, **4**, 3812–3819.

11 G. E. Olifant, V. Mavumengwana, I. A. Hümmelgen and M. A. Mamo, Understanding the sensing mechanism of carbon nanoparticles: MnO_2–PVP composites sensors using *in situ* FTIR—online LCR meter in the detection of ethanol and methanol vapor, *J. Mater. Sci. Mater. Electron*, 2019, **224**, 236–243.

12 S. Mun, Y. Chen and J. Kim, Cellulose-titanium dioxide-multiwalled carbon nanotube hybrid nanocomposite and its ammonia gas sensing properties at room temperature, *Sens. Actuators, B*, 2012, **56**, 87–94.

13 Y. Zhou, T. Zhou, Y. Zhang, L. Tang, Q. Guo and M. Wang, Synthesis of core-shell flower-like WO_3 @ ZIF-71 with enhanced response and selectivity to H_2S gas, *Solid State Ionics*, 2020, **350**, 115278.

14 H. Kim, W. Kim, S. Cho, J. Park and G. Y. Jung, Molecular sieve based on a PMMA/ZIF-8 bilayer for a CO-tolerable H_2 sensor with superior sensing performance, *ACS Appl. Mater. Interfaces*, 2020, **12**, 28616–28623.

15 X. Wu, S. Xiong, Z. Mao, S. Hu and X. Long, A designed ZnO@ZIF-8 core-shell nanorods film as gas sensor with excellent selectivity of H_2 over CO, *Chem. – Eur. J.*, 2017, **10**, 100.

16 D. Matatagui, A. Sainz-Vidal, I. Gracia, E. Figueras, C. Cane and J. M. Saniger, Chemoresistive gas sensor based on ZIF-8/ZIF-67 nanocrystals, *Sens. Actuators, B*, 2018, **274**, 601–608.

17 N. Garg, M. Kumar, N. Kumari, A. Deep and A. L. Sharma, Chemoresistive room-temperature sensing of ammonia using zeolite imidazole framework and reduced graphene oxide (ZIF-67/RGO) composite, *ACS Omega*, 2020, **5**, 27492–27501.

18 L. Malepe, D. T. Ndinteh, P. Ndungu and M. A. Mamo, Selective detection of methanol vapour from

Open Access Article. Published on 16 Februari 2023. Downloaded on 16/10/2025 6:51:59 PTG.
This article is licensed under a Creative Commons Attribution-NonCommercial 3.0 Unported Licence.

a multicomponent gas mixture using a CNPs/ZnO@ZIF-8 based room temperature solid-state sensor, *RSC Adv.*, 2022, **12**, 27094.

19 G. Chen, S. He, G. Shi, Y. Ma, C. Ruan, Q. Chen, X. Jin, X. Liu, H. Dai, X. Chen and D. Huang, *In situ* immobilization of ZIF-67 on wood aerogel for effective removal of tetracycline from water, *Chem. Eng. J.*, 2021, **423**, 130184.

20 S. Perumbilavil, P. Sankar, T. P. Rose and R. Philip, White light Z-scan measurements of ultrafast optical nonlinearity in reduced graphene oxide nanosheets in the 400–700 nm region, *Appl. Phys. Lett.*, 2015, **107**, 051104.

21 Y. Lu, H. Pan, J. Lai, Y. Xia, L. Chen, R. Liang, G. Yan and R. Huang, Bimetallic CoCu-ZIF material for efficient visible light photocatalytic fuel denitrification, *RSC Adv.*, 2022, **12**, 12702–12709.

22 K. A. Lin and S. Chen S, Catalytic reduction of bromate using ZIF-derived nanoscale cobalt/carbon cages in the presence of sodium borohydride, *ACS Sustainable Chem. Eng.*, 2015, **3**, 3096–3103.

23 Z. Ozturk, M. Filez and B. M. Weckhuysen, Decoding nucleation and growth of zeolitic imidazolate framework thin films with atomic force microscopy and vibrational spectroscopy, *Chem. – Eur. J.*, 2017, **23**, 10915–10924.

24 H. Liu, F. Wang, K. Hu, B. Zhang, L. He and Q. Zhou, Superior hydrogen sensing property of porous NiO/SnO_2 nanofibers synthesized *via* carbonization, *Nanomaterials*, 2019, **9**, 1250.

25 H. Guo, Z. Zhang, Z. Jiang, M. Chen, H. Einaga and W. Shangguan, Catalytic activity of porous manganese oxides for benzene oxidation improved *via* citric acid solution combustion synthesis, *J. Environ. Sci.*, 2020, **98**, 196–204.

26 W. Zhang, Y. Chen, L. Zhang, J. Feng, X. Li and A. Wang, Theophylline-regulated pyrolysis synthesis of nitrogen-doped carbon nanotubes with iron-cobalt nanoparticles for greatly boosting oxygen reduction reaction, *J. Colloid Interface Sci.*, 2022, **626**, 653–661.

27 Z. Han, J. Feng, Y. Yao, Z. Wang, L. Zhang and A. Wang, Mn, N, P-tridoped bamboo-like carbon nanotubes decorated with ultrafine Co2P/FeCo nanoparticles as bifunctional oxygen electrocatalyst for long-term rechargeable Zn-air battery, *J. Colloid Interface Sci.*, 2021, **590**, 330–340.

28 J. Ran, H. Chen, S. Bi, Q. Guo, Z. Deng, G. Cai, D. Cheng, X. Tang and X. Wang, One-step *in situ* growth of zeolitic imidazole frameworks-8 on cotton fabrics for photocatalysis and antimicrobial activity, *Cellulose*, 2020, **27**, 10447–10459.

29 S. Saghir and Z. Xiao, Synthesis of novel Ag@ZIF-67 rhombic dodecahedron for enhanced adsorptive removal of antibiotic and organic dye, *J. Mol. Liq.*, 2021, **328**, 115323.

30 N. Dennler, S. Rastogi, J. Fonollosa, A. van Schaik and M. Schmuker, Drift in a .popular metal oxide sensor dataset reveals limitations for gas classification benchmarks, *Sens. Actuators, B*, 2022, **361**, 131668.

31 G. Korotcenkov and B. K. Cho, Instability of metal oxide-based conductometric gas sensors and approaches to stability improvement (short survey), *Sens. Actuators, B*, 2011, **156**, 527–538.

32 M. Z. Abidin, A. Asmat and M. N. Hamidon, Comparative Study of Drift Compensation Methods for Environmental Gas Sensors, *IOP Conf. Ser.: Earth Environ. Sci.*, 2018, **117**, 012031.

33 J. W. Gardner, M. Z. Iskandarani and B. Bott, Effect of electrode geometry on gas sensitivity of lead phthalocyanine thin films, *Sens. Actuators, B*, 1992, **9**(2), 133.

34 J. W. Gardner, A Non-Linear diffusion-reaction model of electrical conduction in semiconductor gas sensors, *Sens. Actuators, B*, 1990, **1**(1), 166.

35 K. C. Ho and Y. H. Tsou, Chemiresistor-Type NO gas sensor based on nickel phthalocyanine thin films, *Sens. Actuators, B*, 2001, **77**(1), 253.

36 S. Kanaparthi and S. G. Singh, Reduction of the measurement time of a chemiresistive gas sensor using transient analysis and the cantor pairing function, *ACS Meas. Sci. Au*, 2022, **2**, 113.

37 J. Wang, P. Yang and X. Wei, High-performance, room-temperature, and no-humidity-impact ammonia sensor based on heterogeneous nickel oxide and zinc oxide nanocrystals, *ACS Appl. Mater. Interfaces*, 2015, **7**, 3816.

38 T. A. Blank, L. P. Eksperiandova and K. N. Belikov, Recent trends of ceramic humidity sensors development: A review, *Sens. Actuators, B*, 2016, **228**, 416–442.

39 X. Zhou, X. Li, H. Sun, P. Sun, X. Liang, F. Liu, X. Hu and G. Lu, Nanosheet-assembled $ZnFe_2O_4$ hollow microspheres for high-sensitive acetone sensor, *ACS Appl. Mater. Interfaces*, 2015, **7**, 15414–15421.

40 Y. Cheng, Y. He, S. Li, Y. Wang, Y. Zhao, Y. Li, H. Li and L. Liu, Ultra-sensitive and selective acetone gas sensor with fast response at low temperature based on Cu-doped α-Fe_2O_3 porous nanotubes, *J. Mater. Sci.: Mater. Electron.*, 2018, **29**, 11178–11186.

41 R. Xing, K. Sheng, L. Xu, W. Liu, J. Song and H. Song, Three-dimensional In_2O_3–CuO inverse opals: synthesis and improved gas sensing properties towards acetone, *RSC Adv.*, 2016, **6**, 57389.

42 S. A. Hakim, Y. Liu, G. S. Zakharovab and W. Chen, Synthesis of vanadium pentoxide nanoneedles by physical vapour deposition and their highly sensitive behavior towards acetone at room temperature, *RSC Adv.*, 2015, **5**, 23489.

43 T. Zhou, S. Chen, X. Wang, C. Xie and D. Zeng, Catalytic activation of cobalt doping sites in ZIF-71-coated ZnO nanorod arrays for enhancing gas-sensing performance to acetone, *ACS Appl. Mater. Interfaces*, 2020, **12**, 48948–48956.

44 A. Dey, Semiconductor metal oxide gas sensors: A review, *Mater. Sci. Eng. B*, 2018, **229**, 206–217.

45 M. Weber, J. H. Kim, J. H. Lee, J. Y. Kim, I. Iatsuns, E. Coy, M. Drobek, A. Julbe, M. Bechelany and S. S. Kim, High-performance nanowire hydrogen sensors by exploiting the synergistic effect of Pd nanoparticles and metal–organic framework membranes, *ACS Appl. Mater. Interfaces*, 2018, **10**, 34765–34773.

46 L. Malepe, P. Ndungu, D. T. Ndinteh and M. A. Mamo, Nickel oxide-carbon soot-cellulose acetate nanocomposite for the

 © 2023 The Author(s). Published by the Royal Society of Chemistry

Open Access Article. Published on 16 Februari 2023. Downloaded on 16/10/2025 6:51:59 PTG.
This article is licensed under a Creative Commons Attribution-NonCommercial 3.0 Unported Licence.

detection of mesitylene vapour: Investigating the sensing mechanism using an LCR Meter coupled to an FTIR spectrometer, *Nanomaterial*, 2022, **12**, 727.

47 Z. Song, Z. Wei, B. Wang, Z. Luo, S. Xu, W. Zhang, H. Yu, M. Li, Z. Huang, J. Zang, F. Yi and H. Liu, Sensitive room-temperature H_2S gas sensors employing SnO_2 quantum wire/reduced graphene oxide nanocomposites, *Chem. Mater.*, 2016, **28**, 1205–1212.

48 K. Isokoski, C. Poteet and H. Linnartz, Highly resolved infrared spectra of pure CO2 ice (15–75 K), *Astron. Astrophys.*, 2013, **555**, 85.

49 T. Schädle, B. Pejcic and B. Mizaikoff, Monitoring dissolved carbon dioxide and methane in brine environments at high pressure using IR-ATR spectroscopy, *Anal. Methods*, 2016, **8**(4), 756–762.

50 L. Malepe, D. T. Ndinteh and M. A. Mamo, The effect of measurement parameters on the performance of the sensors in the detection of organic compound vapours, *Chem. Phys. Impact*, 2022, **4**, 100068.